Int. J. Heat Mass Transfer. Vol. 34, No. 6, pp. 1525–1542, 1991
Printed in Great Britain

0017–9310/91 $3.00 + 0.00

An experimental and numerical simulation of mixed convection in large baffled rectangular chambers

K. L. YERKES† and A. FAGHRI
Department of Mechanical and Materials Engineering, Wright State University, Dayton, OH 45435, U.S.A.

(*Received* 6 *April* 1990 *and in final form* 24 *July* 1990)

Abstract—The effects of mixed convection within large baffled chambers for both 'aided' and 'opposed' buoyant forces are investigated. Experimental and numerical results are compared for the momentum boundary layer thickness and temperature distribution within the chamber. Two- and three-dimensional transient laminar numerical models are formulated using a fully implicit finite-difference scheme. The inlet and wall temperatures are held constant while maintaining a uniform inlet velocity. Two tiers of four (two per tier) horizontal baffles are located axisymmetrically about the vertical axis with the inlet at the top and exhaust at the base of the chamber. The difference between the inlet and wall temperatures ranges between -1.0 and 3.3°C with a Prandtl number, $Pr = 0.7$, inlet Reynolds number, $Re = 32$ and 235, and inlet Rayleigh number, $Ra = 0$–6.8×10^7. It is concluded that the flow is predominantly buoyant and asymmetric in nature. The development of the flow is sensitive to small variations in the temperature difference between the inlet and wall.

INTRODUCTION

LARGE baffled rectangular chambers with low inlet velocities, as shown in Fig. 1(a), have traditionally been used to study a variety of chemical atmospheres generated for studies of health effects, chemical reaction and chemical species formation, and aerosol characterization. Generally, they have a cross-sectional diameter greater than 0.5 m with an inlet velocity set to maintain 10–15 chamber volume changes per hour. The inlet and exhaust may be mounted vertically or horizontally with an array of internal baffles included for atmosphere dispersion purposes.

Rayleigh–Bénard flow in confined and partially open enclosures with and without baffles or dividers has been studied extensively [1–4]. These experimental and numerical investigations have determined the temperature profile and flow structure in various closed cavity geometries with different Grashof, Prandtl, and Rayleigh number ranges. Other investigations have concerned mixed convective flow in pipes [5], inclined tubes [6], vertical channels [7], spherical annuli [8], and vertical and horizontal plates [9–12], but there is little information with regard to mixed convective flow in large baffled chambers.

Studies concerning mixed convection in heated vertical channels have shown the effects of 'aided' and 'opposed' buoyant forces in larger geometries. Yao [7] demonstrated that the 'aided' buoyant forces for upward vertical channel flow tended to accelerate the boundary layer such that incoming flow was drawn toward the channel wall. Tanaka *et al.* [5] also showed an increase in the wall boundary layer velocity with a decrease in Reynolds number for the case of 'aided' buoyant forces in a uniformly heated pipe. These investigations indicate a shift in the major velocity component toward the pipe or channel walls as buoyant forces become significant. While some effects of buoyant forces were indicated, the chambers of interest in addition to including baffles, also have inlet Reynolds numbers that are one to two orders of magnitude lower, resulting in a flow structure that is predominantly buoyant in nature.

Initial investigations of these chambers incorporated flow visualization techniques to optimize the chamber geometry so that well-dispersed atmospheres could be obtained [13, 14]. Quantitative studies have determined the mean residence time of a chamber, the rate of dispersion of a tracer gas, and the distribution of vapors, droplets, and solid particles [15–18]. Cholette and Cloutier [19] addressed various mixing conditions in chambers by observing deviations in the rate of decay from a perfectly mixed condition, which were characterized as non-idcal mixing resulting from plug or piston flow, short-circuit flow, and stagnant regions. Kimmel *et al.* [20] applied the techniques developed by Cholette and Cloutier [19] in analyzing and quantifying the transport of various compounds. These investigations, however, have not addressed the effects of mixed convection on heat and mass transfer within these chambers, which is of interest to better understand their operation and provide a basis for improvement, modification and future development.

A typical chamber consists of a conical inlet

† Present address: Wright Research and Development Center, Wright–Patterson AFB, OH 45433, U.S.A.

NOMENCLATURE

A_1	aspect ratio, L/H
A_2	aspect ratio, L/D
A_3	aspect ratio, D_h/H
$\mathbf{B}_z$	body force vector in the z-direction
C_p	specific heat [J kg^{-1} °C^{-1}]
D	depth of chamber [m]
D_h	hydraulic diameter, $2LD/(L+D)$ [m]
g	acceleration due to gravity [m s^{-2}]
Gr	Grashof number, $g\beta D_h^3 \delta T/\nu^2$
H	height of chamber [m]
h	hydrostatic height [m]
k	thermal conductivity [W m^{-1} °C^{-1}]
L	width of chamber [m]
P	non-dimensional pressure, $(p^+ - p_0^+)/\rho W_{IN}^2$
p^+	dimensional pressure, due to motion and hydrostatic pressures, $p^+ = p^* - \rho gh$ [N m^{-2}]
p^*	dimensional pressure due to motion (static pressure) [N m^{-2}]
Pr	Prandtl number, $\mu C_p/k$
Q_{IN}	inlet volumetric flow rate [m^3 s^{-1}]
Ra	Rayleigh number, $Gr \cdot Pr$
Re	inlet Reynolds number, $D_h W_{IN}/\nu$
T'	non-dimensional temperature, $(T_{IN} - T)/(T_{IN} - T_w)$
T	temperature [°C]
T_{IN}	inlet temperature [°C]
T_{sw}	side wall temperature (see Fig. 1) [°C]
T_w	end wall temperature (see Fig. 1) [°C]
t	time [s]
U	non-dimensional x-direction velocity, u/W_{IN}
u	x-direction velocity [m s^{-1}]
V	non-dimensional y-direction velocity, v/W_{IN}
V_{ch}	chamber volume [m^3]
V_{max}	magnitude of maximum velocity [m s^{-1}]
v	y-direction velocity [m s^{-1}]
W	non-dimensional z-direction velocity, w/W_{IN}
w	z-direction velocity [m s^{-1}]
W_{IN}	inlet vertical velocity [m s^{-1}]
X	non-dimensional horizontal coordinate, x/D
x	horizontal coordinate [m]
Y	non-dimensional horizontal coordinate, y/L
Y'	experimental horizontal coordinate axis about chamber centerline, $(y - L/2)/(L/2)$
y	horizontal coordinate [m]
Z	non-dimensional vertical coordinate, z/H
z	vertical coordinate [m].

Greek symbols

β	coefficient of thermal expansion, $-(1/\rho)(\partial\rho/\partial T)$ [K^{-1}]
δ	boundary layer thickness [m]
δT	$(T_{IN} - T_w)$ [°C]
ε	fractional change in dependent variable
θ	non-dimensional time, tQ_{IN}/V_{ch}
μ	dynamic viscosity [kg m^{-1} s^{-1}]
ν	kinematic viscosity, μ/ρ [m^2 s^{-1}]
ρ	fluid density [kg m^{-3}]
ϕ	dependent variable
ϕ_s	dependent variable at specific sweep or time step.

intended to uniformly distribute the atmosphere of interest across the inlet plane. The exhaust consists of a manifold to achieve a uniform flow across the exhaust plane. Inlet and exhaust flow rates are controlled independently to maintain a slight negative chamber pressure with respect to the ambient pressure (2.5–5.1 cm H_2O).

This investigation considers the development of the flow structure due to a temperature gradient between the inlet and wall temperature. Table 1 shows the scope of this investigation with both two-dimensional (2-D) and three-dimensional (3-D) numerical formulations (cases 1–6) and experimental results from a scaled-down laboratory experimental model (case 7), which will be used in the analysis of the larger, full-size chamber. The 3-D effects of the experimental model were considered and the corresponding 3-D numerical solutions used to account for discrepancies between the experimental and 2-D numerical results. The 2-D numerical formulation corresponds to the larger, full-size chamber with a depth of 1 m and was compared to the experimental results. The vertical wall temperature, T_w, was assumed to be constant due to the thin wall construction. Typical ranges of Reynolds, Grashof, Rayleigh and Prandtl numbers at the inlet plane are also shown in Table 1, where the characteristic length is the hydraulic diameter of the chamber body. The 2-D numerical results were further divided into three distinct flow types and defined as short-circuit (convection) flow, mixed (mixed convection) flow, and dead space (diffusion) flow and compared to the data obtained by Kimmel *et al.* [20] using a similar chamber and the method developed by Cholette and Cloutier [19].

Initial verification of the magnitude of the buoyant force compared to inertia forces was determined by evaluating Gr/Re^2 at the inlet plane. The buoyant force was found to dominate the inertia forces by as much as three orders of magnitude with a temperature difference of $\delta T = 1.0$°C. The buoyant force, there-

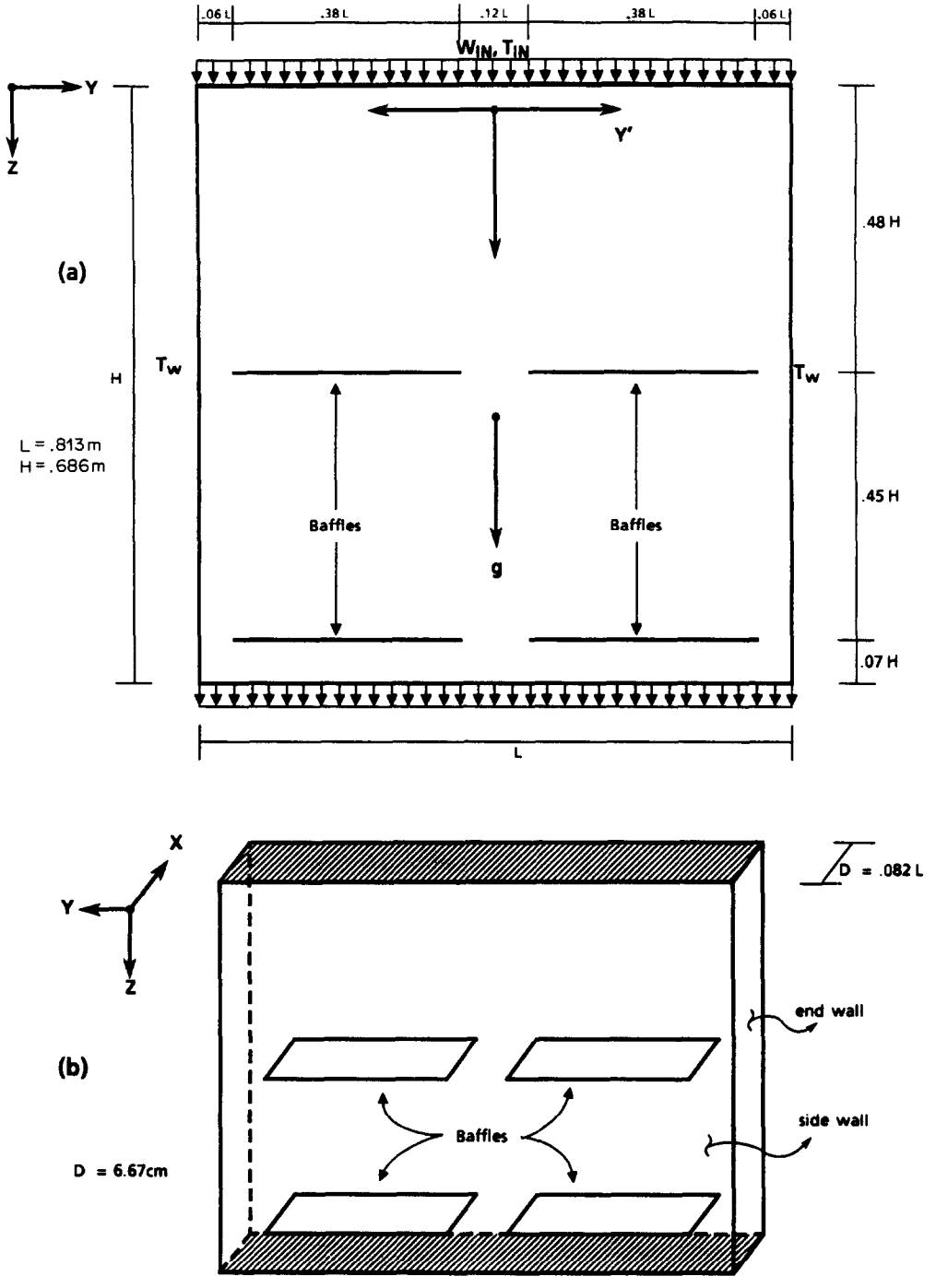

FIG. 1. Chamber geometry specifications: (a) two-dimensional geometry; (b) three-dimensional laboratory model geometry.

fore, must be considered as the primary force in the development of the flow structure.

ANALYSIS

Numerical solutions of the 2-D and 3-D incompressible time-dependent laminar Navier–Stokes equations were considered. The time-dependent approach was chosen to evaluate the presence of a steady periodic oscillation. The 2-D and 3-D problems shown in Fig. 1 were considered with the 3-D formulation simulating the experimental model.

For this investigation, only the dimensional form of the governing equations was solved, thereby circumventing the need for scaling considerations of the non-dimensional parameters as is typically required

Table 1. Parametric specifications for numerical and experimental investigation

Case	Approach	T_{sw}	T_w (°C)	T_{IN} (°C)	δT (°C)
1	2-D numerical	N/A	24	24	0
2	2-D numerical	N/A	24	23	−1
3	2-D numerical	N/A	24	25	1
4	2-D numerical	N/A	24	27.3	3.3
5	3-D numerical	adiabatic	24	27.3	3.3
6	3-D numerical	constant†	24	27.3	3.3
7	3-D experimental	conducting	24	27.3	3.3

Case	Ra	Gr	Re	A_1	A_2	A_3
1	0	0	235	1.19	0.813	1.31
2	$(-)6.82\times10^7$‡	$(-)9.74\times10^7$	235	1.19	0.813	1.31
3	6.82×10^7	9.74×10^7	235	1.19	0.813	1.31
4	2.25×10^8	3.21×10^8	235	1.19	0.813	1.31
5	5.84×10^5	8.35×10^5	32.3	1.19	12.2	0.180
6	5.84×10^5	8.35×10^5	32.3	1.19	12.2	0.180
7	5.84×10^5	8.35×10^5	32.3	1.19	12.2	0.180

† $T_{sw}=(T_{IN}-\delta T/6)$ or $T'=1/6$.

‡ Negative sign signifies 'opposed' buoyant force at vertical 'end walls'; otherwise, 'aided'.

$Pr=0.7$, $W_{IN}=4.1\times10^{-3}$ m s^{-1}.

for buoyant flow conditions [1]. The non-dimensional form of the governing equations was derived using the length scale and characteristic velocity generally chosen for mixed convection pipe flow and the resultant non-dimensional parameters were compared using subsequent dimensional solutions.

The Boussinesq approximation was used in the vertical direction to account for buoyancy effects. Using this approximation the vertical body force becomes $\mathbf{B}_z=\rho\mathbf{g}[1-\beta(T-T_{IN})]$, where $\beta=1/T_{IN}$ for an ideal gas. The reference values for all gas properties were taken at the inlet plane.

The chamber inlet cone was assumed to provide a uniform velocity distribution across the inlet plane with the exhaust manifold providing a velocity distribution resulting from a constant exhaust pressure across the outlet plane. Viscous dissipation and pressure work were assumed to be negligible due to the low buoyancy-induced velocities. With these assumptions, the 3-D governing equations become:

Conservation of mass

$$\frac{\partial u}{\partial x}+\frac{\partial v}{\partial y}+\frac{\partial w}{\partial z}=0. \tag{1}$$

Conservation of momentum

$$\rho\left(\frac{\partial u}{\partial t}+u\frac{\partial u}{\partial x}+v\frac{\partial u}{\partial y}+w\frac{\partial u}{\partial z}\right)=-\frac{\partial p^*}{\partial x}+\mu\left(\frac{\partial^2 u}{\partial x^2}+\frac{\partial^2 u}{\partial y^2}+\frac{\partial^2 u}{\partial z^2}\right) \tag{2}$$

$$\rho\left(\frac{\partial v}{\partial t}+u\frac{\partial v}{\partial x}+v\frac{\partial v}{\partial y}+w\frac{\partial v}{\partial z}\right)=-\frac{\partial p^*}{\partial y}+\mu\left(\frac{\partial^2 v}{\partial x^2}+\frac{\partial^2 v}{\partial y^2}+\frac{\partial^2 v}{\partial z^2}\right) \tag{3}$$

$$\rho\left(\frac{\partial w}{\partial t}+u\frac{\partial w}{\partial x}+v\frac{\partial w}{\partial y}+w\frac{\partial w}{\partial z}\right)=-\frac{\partial p^*}{\partial z}+\mu\left(\frac{\partial^2 w}{\partial x^2}+\frac{\partial^2 w}{\partial y^2}+\frac{\partial^2 w}{\partial z^2}\right)+\rho g\beta(T-T_{IN}). \tag{4}$$

Conservation of energy

$$\rho\left(\frac{\partial T}{\partial t}+u\frac{\partial T}{\partial x}+v\frac{\partial T}{\partial y}+w\frac{\partial T}{\partial z}\right)=\frac{k}{C_p}\left(\frac{\partial^2 T}{\partial x^2}+\frac{\partial^2 T}{\partial y^2}+\frac{\partial^2 T}{\partial z^2}\right). \tag{5}$$

The non-dimensional form of the governing equations can be derived in terms of the aspect ratios: A_1, A_2, and A_3.

Conservation of mass

$$A_2\frac{\partial U}{\partial X}+\frac{\partial V}{\partial Y}+A_1\frac{\partial W}{\partial Z}=0. \tag{6}$$

Conservation of momentum

$$\frac{\partial U}{\partial\theta}+\left(\frac{A_2}{A_1}U\frac{\partial U}{\partial X}+\frac{1}{A_1}V\frac{\partial U}{\partial Y}+W\frac{\partial U}{\partial Z}\right)=-\frac{A_2}{A_1}\frac{\partial P}{\partial X}+\frac{A_3}{Re}\left(\left(\frac{A_2}{A_1}\right)^2\frac{\partial^2 U}{\partial X^2}+\frac{1}{A_1^2}\frac{\partial^2 U}{\partial Y^2}+\frac{\partial^2 U}{\partial Z^2}\right) \tag{7}$$

$$\frac{\partial V}{\partial \theta}+\left(\frac{A_2}{A_1}U\frac{\partial V}{\partial X}+\frac{1}{A_1}V\frac{\partial V}{\partial Y}+W\frac{\partial V}{\partial Z}\right)$$
$$=-\frac{1}{A_1}\frac{\partial P}{\partial Y}+\frac{A_3}{Re}\left(\left(\frac{A_2}{A_1}\right)^2\frac{\partial^2 V}{\partial X^2}+\frac{1}{A_1^2}\frac{\partial^2 V}{\partial Y^2}+\frac{\partial^2 V}{\partial Z^2}\right) \quad (8)$$

$$\frac{\partial W}{\partial \theta}+\left(\frac{A_2}{A_1}U\frac{\partial W}{\partial X}+\frac{1}{A_1}V\frac{\partial W}{\partial Y}+W\frac{\partial W}{\partial Z}\right)$$
$$=-\frac{\partial P}{\partial Z}+\frac{A_3}{Re}\left(\left(\frac{A_2}{A_1}\right)^2\frac{\partial^2 W}{\partial X^2}+\frac{1}{A_1^2}\frac{\partial^2 W}{\partial Y^2}+\frac{\partial^2 W}{\partial Z^2}\right)+\frac{Gr\,T'}{A_3\,Re^2}. \quad (9)$$

Conservation of energy

$$\frac{\partial T'}{\partial \theta}+\left(\frac{A_2}{A_1}U\frac{\partial T'}{\partial X}+\frac{1}{A_1}V\frac{\partial T'}{\partial Y}+W\frac{\partial T'}{\partial Z}\right)$$
$$=\frac{A_3}{Pr\cdot Re}\left(\left(\frac{A_2}{A_1}\right)^2\frac{\partial^2 T'}{\partial X^2}+\frac{1}{A_1^2}\frac{\partial^2 T'}{\partial Y^2}+\frac{\partial^2 T'}{\partial Z^2}\right). \quad (10)$$

The boundary conditions specify a uniform inlet velocity profile and a constant vertical end wall temperature. The side walls were either at a fixed temperature, $(T')_{sw}=1/6$, or adiabatic, $(\partial T'/\partial X)_{sw}=0$, for the 3-D formulation. The magnitude of the inlet velocity is specified, but the outlet velocity is set by satisfying the conservation of mass with a constant reference pressure across the outlet plane. The boundary conditions become:

$$X=0,\quad 0\leqslant Y\leqslant 1,\quad 0\leqslant Z\leqslant 1,$$
$$(\partial T'/\partial X)=0 \text{ or } T'=1/6,$$
$$U=0,\quad V=0,\quad W=0$$
$$X=1,\quad 0\leqslant Y\leqslant 1,\quad 0\leqslant Z\leqslant 1,$$
$$(\partial T'/\partial X)=0 \text{ or } T'=1/6,$$
$$U=0,\quad V=0,\quad W=0$$
$$Y=0,\quad 0\leqslant X\leqslant 1,\quad 0\leqslant Z\leqslant 1,$$
$$T'=1,\quad U=0,\quad V=0,\quad W=0$$
$$Y=1,\quad 0\leqslant X\leqslant 1,\quad 0\leqslant Z\leqslant 1,$$
$$T'=1,\quad U=0,\quad V=0,\quad W=0$$
$$Z=0,\quad 0\leqslant X\leqslant 1,\quad 0\leqslant Y\leqslant 1,$$
$$T'=0,\quad U=0,\quad V=0,\quad W=1$$
$$Z=1,\quad 0\leqslant X\leqslant 1,\quad 0\leqslant Y\leqslant 1,$$
$$U=0,\quad V=0,\quad P=0.$$

The outlet boundary condition for temperature was considered to be locally parabolic such that the Peclet number is sufficiently large so as to exhibit local one-way behavior in the axial direction [21]. The baffles were treated as being infinitesimally thick with a no-slip boundary condition. The baffle temperature was specified to be equal to the local fluid temperature.

NUMERICAL SCHEME

The numerical scheme was a finite-difference iterative method using the control-volume approach [22]. The 2-D and 3-D numerical models were formulated using the fully implicit, time-dependent, laminar Navier–Stokes equations. The 'SIMPLEST' [22] method was used for the momentum equations with the hybrid differencing formulation. When a cell Peclet number is within the range -2 to 2, a central-difference scheme is used; otherwise, the upwind differencing scheme is used. The no-slip boundary condition on the walls and baffles was specified by setting the cell velocity to zero.

The solution sequence involved solving for the velocity and temperature fields from an assumed pressure field at a specific time step. The pressure field was then updated using these velocity and temperature fields in the pressure-correction equation such that the conservation of mass was satisfied. This iterative sweep process was then repeated using a slab-by-slab method at each time step until convergence criteria were satisfied. Convergence characteristics at each time step were maintained by reducing the time step where appropriate with the minimum computational time required to reach a steady state solution being at least three characteristic times, H/W_{IN}, or approximately 10 min. In addition, conditions for convergence to a solution, either at a specific time step or to a steady state solution, were based upon a dependent variable, ϕ, varying less than a predetermined change of the magnitude fraction, ε_ϕ, between successive sweeps or time steps where

$$|\phi_s-\phi_{s+1}|/\phi\leqslant\varepsilon_\phi.$$

The values of ε_ϕ were varied and it was required that the magnitude of the dependent variable be greater than the roundoff error or truncation error such as would happen when velocities approach zero. Typically, for a steady state solution, ε_ϕ ranged from 10^{-3} to 10^{-2} over a time span of 25 s, while over five successive sweeps ε_ϕ was less than 10^{-3}. Intermediate results were monitored to ensure convergence and numerical stability at a specific time step during the course of the solution. These intermediate results were also used to determine convergence toward either a steady state or a steady periodic solution.

Appropriate grid size and spacing were chosen to give acceptable numerical accuracy while still maintaining reasonable computational times. Generally, the approach to organizing the grid layout for typical closed cavity buoyant problems has been to concentrate grids at the walls to accurately describe the thermal and momentum boundary layers. For the 2-D formulation, a uniform 100×100 grid was chosen to give good coverage without knowing in advance as

to where the greatest dependent variable gradients would be located within the chamber cavity. This grid layout was subsequently refined in regions of interest to verify numerical accuracy. By doubling the grid number at the vertical wall, which was a region with large gradients, the maximum boundary layer velocity was changed by less than 3%. The momentum boundary layer thickness was changed by less than 5% for boundary layer thicknesses greater than 2.5 cm and the temperature was changed by less than 1%.

While the 100×100 grid in the 2-D formulation was found to be satisfactory, expansion to a 3-D formulation was found to be computationally intensive and time consuming. The grid number in the third dimension was set to five to maintain reasonable computational times while still being able to qualitatively describe the general flow structure for the x–z plane and thereby address some of the inconsistencies between the numerical and experimental results.

The Nusselt number was not evaluated since this only gives information regarding gross behavior and is insensitive to specific information regarding the flow structure and temperature distribution at various chamber locations such as the core region [1]. This did not preclude evaluation of the Nusselt number to verify numerical convergence and optimum grid size but still only gave information for the numerical conditions at the chamber wall. In addition, there is an error associated with the Boussinesq approximation [23] in which there is as much as a 20% overestimation of the maximum vertical velocity.

EXPERIMENTAL APPROACH

An experimental chamber model was fabricated using 1.91 cm thick Plexiglas with an interior body dimension of $0.813 \text{ m} \times 6.67$ cm and 0.686 m high, as shown in Figs. 1(b) and 2. Baffles of 1.5 mm thick Plexiglas were inserted across the chamber depth and fixed into the vertical side walls. The vertical end walls were fabricated using a thin aluminum plate combined with a water jacket to maintain a constant wall temperature. A Lauda recycling water bath was used to maintain a constant water temperature in the water jacket (± 0.2 C). Inlet and exhaust air was passed through a series of laminated porous stainless steel plates with a nominal pore size of 44 μm to maintain a uniform velocity profile. The inlet volumetric flow rate was adjusted and monitored using a Matheson rotameter and corrected to account for the operational pressure drop. The chamber pressure was maintained to that of ambient by adjusting the exhaust flow rate.

Field temperature measurements were made using

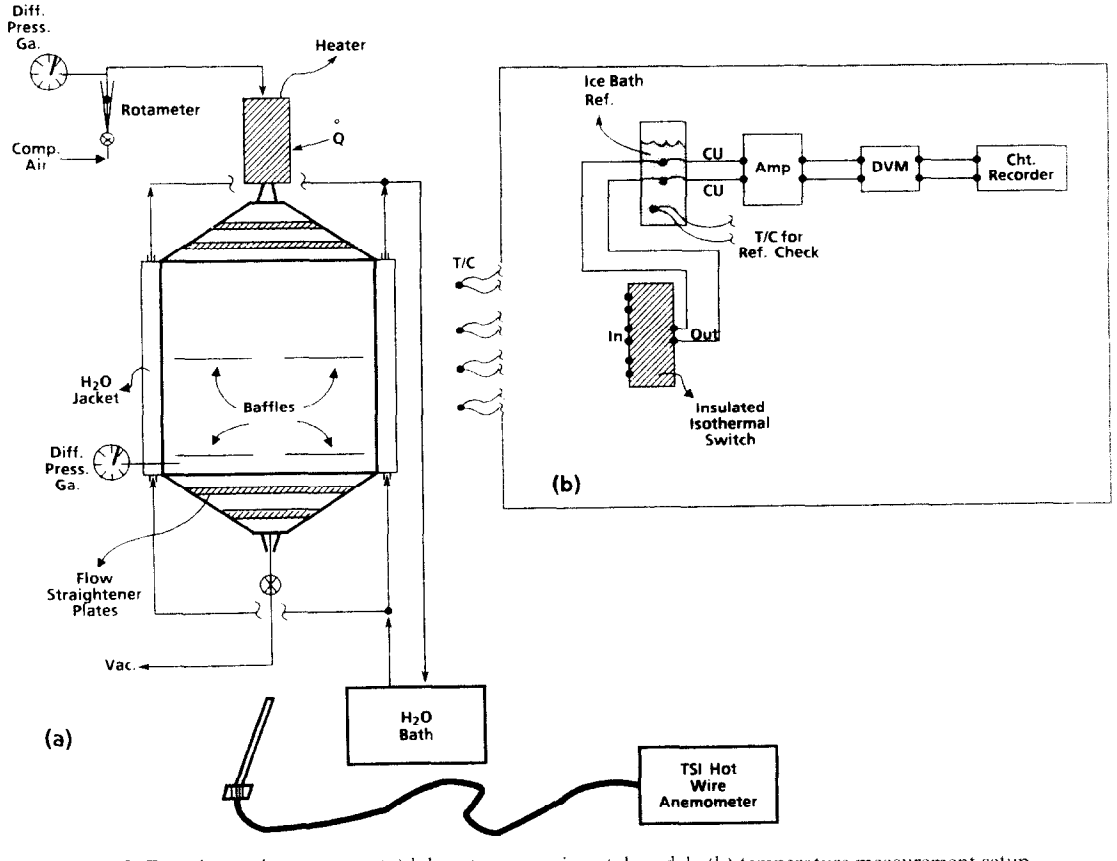

FIG. 2. Experimental apparatus: (a) laboratory experimental model; (b) temperature measurement setup.

iron–constantan exposed junction thermocouples individually calibrated to within $\pm 0.1°C$. Each thermocouple was immersed in a stirred water bath and calibrated using a standard NBS traceable thermometer (Ever Ready Thermometer Co., New York) ($\pm 0.05°C$) over the anticipated range of operation of 24–32°C. An insulated isothermal thermocouple switch to minimize stray e.m.f. and thermocouple amplifier were used in conjunction with a digital voltmeter for a sensitivity greater than the required ± 5.1 μV for $\pm 0.1°C$ measurements. Thermocouple voltages over a range of calibration temperatures were obtained and referenced to an ice point consisting of a large reservoir ice bath with an additional reference thermocouple to verify shifts in the reference ice point temperature. Periodically, the standard NBS traceable thermometer was also used to verify field temperatures. Thermocouples were chosen and sized to minimize flow disturbances and maximize response time with a sheath diameter of 0.159 cm and a bead diameter ranging from 0.025 to 0.076 cm for a time constant of 1.35–1.73 s.

Velocity data were obtained using a TSI IFA-100 hot wire anemometer using a platinum film sensor model 1211–10. To effectively use the hot wire anemometer, the magnitude of the buoyant-induced velocity, due to the heating of the sensor, in relation to the velocity to be measured was of interest. Uncertainty errors can be determined depending upon the orientation of the fluid velocity to that of the induced buoyant velocity [24]. This is evident when the stream velocity is opposed to the sensor-induced buoyant velocity and of the same order of magnitude. During this experiment, there was a range of stream velocities in which the indicated sensor velocity would decrease as the stream velocity increased. This is due to the summing of counteracting velocities and indicating a lower resultant velocity. A spot calibration of the probe sensor using a series of parallel screens at isothermal conditions showed this velocity to be of the order of $2.15 \times 10^{-2} \pm 0.25 \times 10^{-2}$ m s^{-1}. Therefore, hot wire anemometry was limited to the evaluation of the momentum boundary layer thickness along the vertical end wall with the edge of the boundary layer being defined as this baseline velocity.

RESULTS AND DISCUSSIONS

Experimental data consisted of temperature measurements at various chamber locations at the central plane and hot wire anemometry data to determine the momentum boundary layer thickness, which were then compared with the 2-D and 3-D numerical solutions.

To obtain similitude of the full-size chamber using the experimental model, the non-dimensional parameters, A_3/Re, $Gr/(A_3\ Re^2)$ and $A_3/(Pr \cdot Re)$ were matched with the exception of the coefficient, A_2/A_1. The aspect ratio A_2 was not considered and was either 0.813 or 12.2 for the full-size chamber and experimental chamber, respectively. As a result, the inlet velocity, W_{IN}, and temperature difference, δT, between the inlet and vertical end walls remained the same as that of the full-size chamber since only the chamber depth varied.

Figures 3–6 show the chamber velocity direction, velocity magnitude and temperature contours for the 2-D cases 1–4. Figures 7–10 show the temperature contours, and velocity vector and magnitude plots for the 3-D cases 5 and 6. Final comparisons of non-dimensional temperature are shown in Figs. 11 and 12 for the 2-D full-size chamber case 4, the 3-D cases 5 and 6, and experimental results (case 7). Momentum boundary layer thickness and maximum velocity for the cases investigated are shown in Table 2.

Three characteristic flow structures were observed for negative, positive and zero differences between the inlet and vertical wall temperatures. The 3-D cases exhibited additional flow structures inherent to the boundary condition in the third dimension.

Negative differences between the inlet and vertical end wall temperatures induced 'opposed' buoyant forces at the vertical end walls as shown in Figs. 3(b) and 4 for the 2-D case 2. The flow structure consisted of a central downward flowing core of cooler fluid with a reflux of mass at the vertical end walls from the exhaust to the inlet due to the upward vertical velocity component induced by the 'opposed' buoyant forces. This reflux of mass subsequently combines with the cooler inlet mass at the inlet plane. The resulting flow structure was not only steady periodic in nature with

Table 2. Boundary layer thickness and maximum velocity

Case	V_{max}	δ (cm)†			Characteristic
		$Z/H = 0.44$	$Z/H = 0.67$	Error (cm)	
1	2.81×10^{-2}	N/A	N/A	N/A	steady state
2	7.03×10^{-2}	N/A	N/A	N/A	steady periodic
3	6.89×10^{-2}	2.38	2.84	± 0.41	steady state
4	1.03×10^{-1}	1.98	2.32	± 0.41	steady state
5	1.02×10^{-1}	1.93	2.31	± 0.41	steady state
6	1.16×10^{-1}	2.09	2.58	± 0.41	steady state
7	not measured	1.91	2.54	± 0.32	steady state

† δ determined to be the location for a velocity equivalent to the minimum response of the anemometer sensor ($\approx 2.15 \times 10^{-2}$ m s^{-1}).

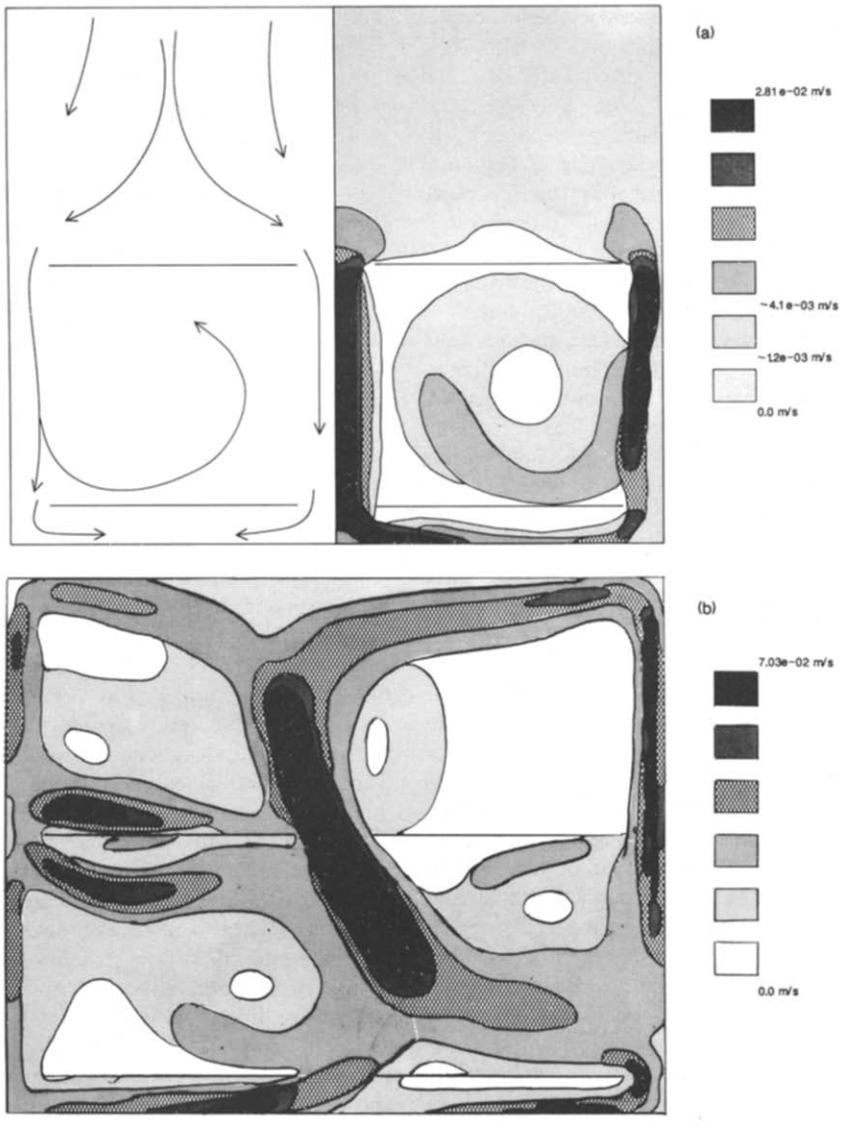

FIG. 3. Two-dimensional numerical results: (a) velocity direction and magnitude profile case 1; (b) velocity magnitude profile case 2.

a period of the order of 300 s, but was also displaced from the expected symmetrical flow pattern. Placement of the lower baffles in relation to the exhaust plane was found to be the contributing factor in the development of the oscillatory flow and the asymmetric flow structure. When these lower baffles were removed, the flow structure became symmetric with little oscillation.

Positive and increasing differences between the inlet and end wall temperatures resulted in an increased downward vertical velocity component at the vertical end walls with mass refluxing from the exhaust plane and flowing horizontally along the upper surface of the lower baffles. This is shown in Figs. 5–7 for the 2-D cases 3 and 4 and the 3-D adiabatic side wall case 5. As the temperature differences increased, both a thinning of the vertical wall boundary layer coupled with an increased vertical velocity component was observed as shown in Table 2. With this increase in the temperature differential, the central vertical mass flow between the baffles was diminished as a result of an increased mass flux to the vertical end walls above the upper baffles.

There are two distinct regions of interest. The first region is above the upper baffles, locations where flow is diverted around the baffles, and along the vertical end walls. In these areas, convection begins to dominate diffusion and becomes the primary mode of energy transport. This is demonstrated in the temperature contour plots of Figs. 5–7 by the constant temperature region and the distorted contours between the baffles and the chamber walls. The second

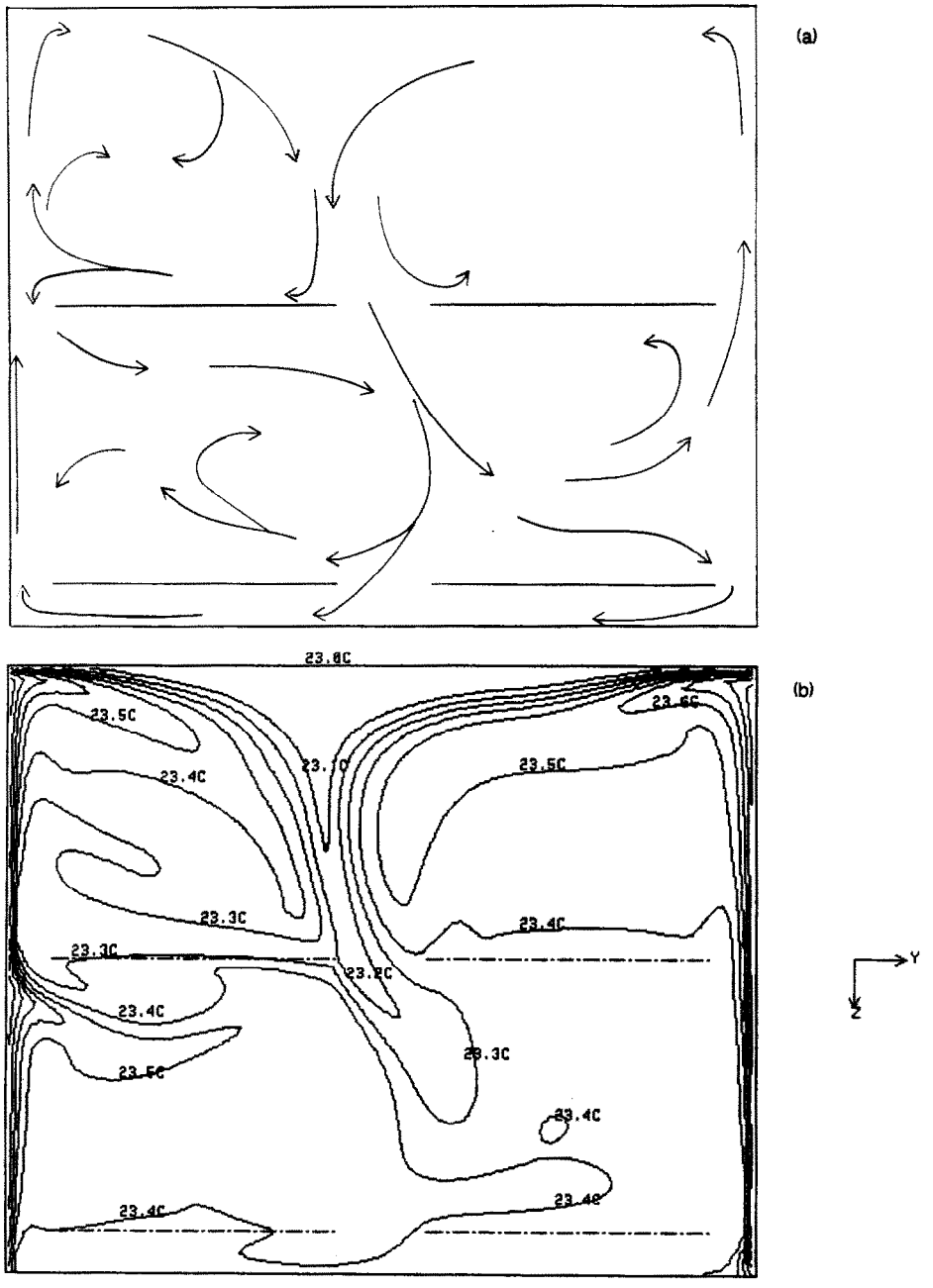

FIG. 4. Two-dimensional numerical results for case 2: (a) chamber velocity direction profile; (b) temperature contour.

region of interest is below the upper baffles and above the lower baffles where diffusion is the primary model of energy transport as a result of the low velocity components. This is demonstrated by the stratified temperature gradient in the contour plots of Figs. 5–7. This second region varies in size and will gradually diminish as the inlet and vertical end wall temperature differences are positive and decreasing to zero. With decreasing positive temperature differences, the central vertical mass flow between the baffles will increase. The mass will enter into the lower region and flow horizontally along the lower surface of the upper baffles toward the vertical end walls. As the temperature difference is further decreased, approaching zero, the flow will approach that of Fig. 3(a) in which the buoyant forces are no longer dominant.

Formulation of the 3-D case was considered such that the additional side walls for the third dimension were either adiabatic (case 5) or constant temperature (case 6). With this formulation, a solution with a conduction side wall boundary condition, as was anticipated using the experimental model, would be

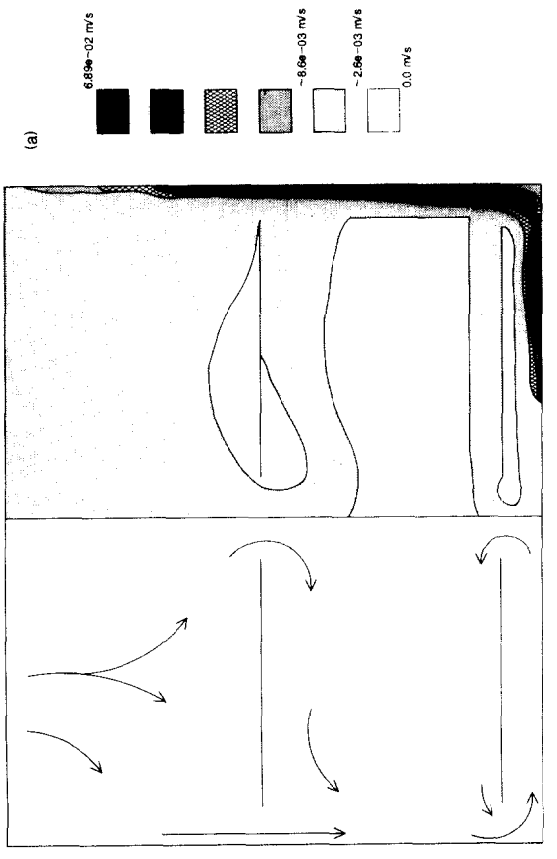

FIG. 5. Two-dimensional numerical results for case 3: (a) chamber velocity direction and magnitude profile; (b) temperature contour.

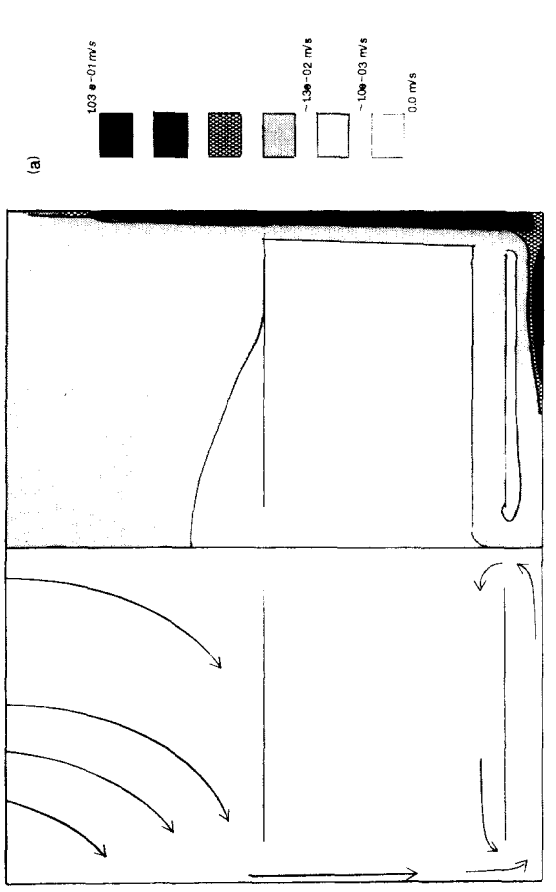

FIG. 6. Two-dimensional numerical results for case 4: (a) chamber velocity direction and magnitude profile; (b) temperature contour.

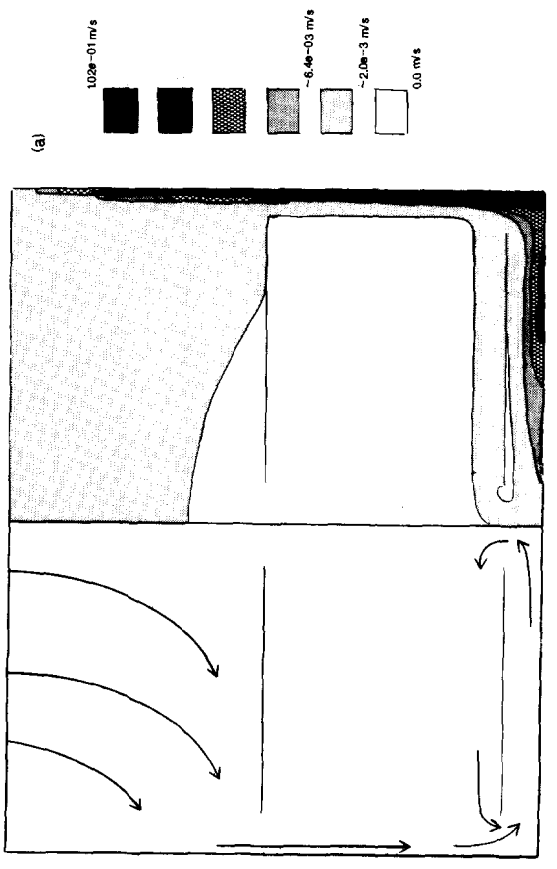

FIG. 7. Three-dimensional numerical results for case 5 at center plane: (a) chamber velocity direction and magnitude profile; (b) temperature contour.

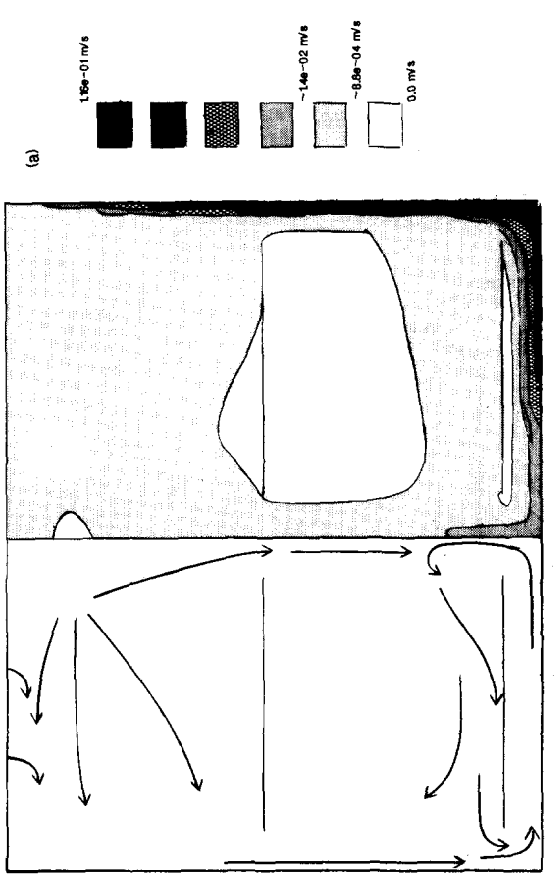

FIG. 8. Three-dimensional numerical results for case 6 at center plane: (a) chamber velocity direction and magnitude profile; (b) temperature contour.

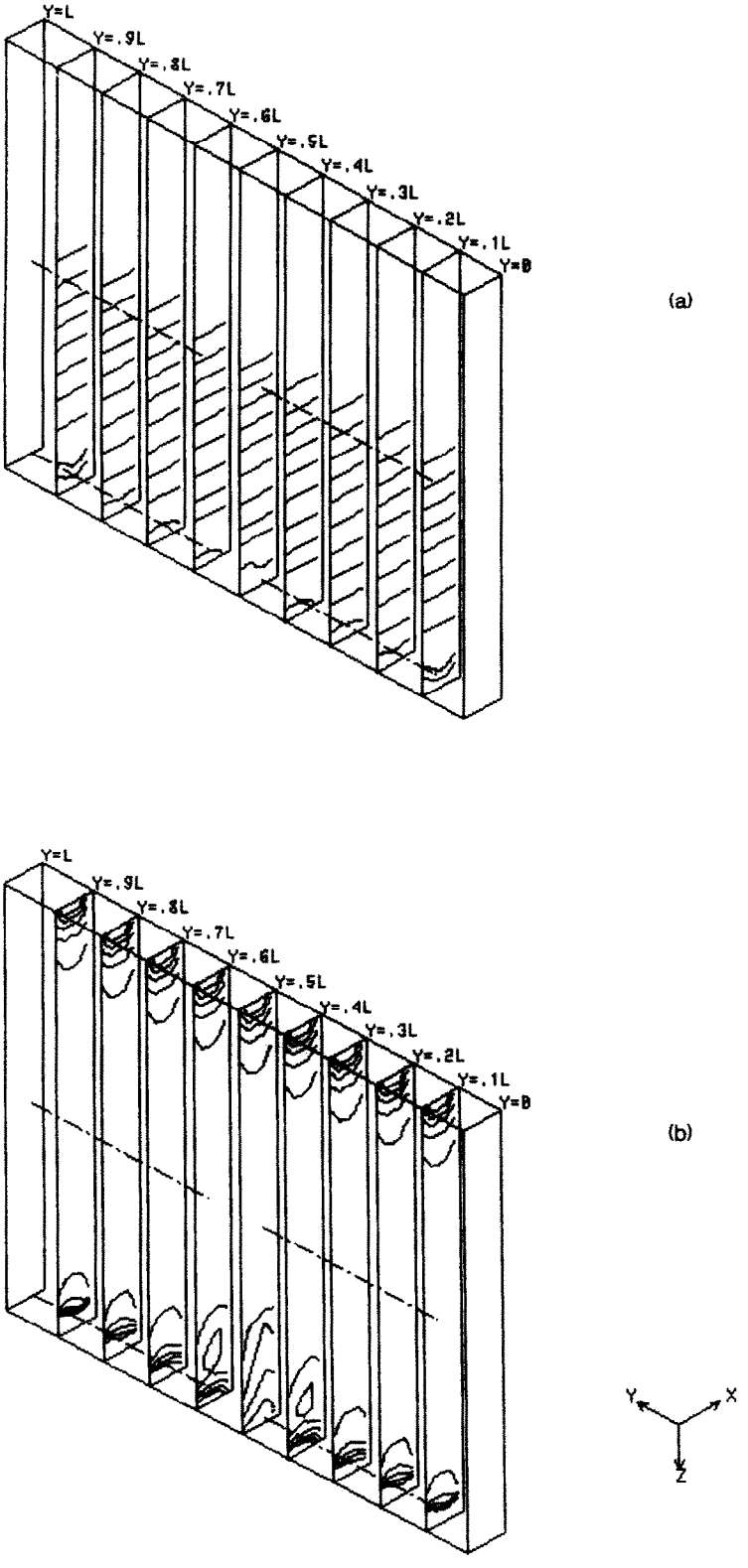

FIG. 9. Three-dimensional numerical results, temperature contour: (a) case 5, 25.3–27.3°C at 0.2°C intervals; (b) case 6, 26.3–27.3°C at 0.1°C intervals.

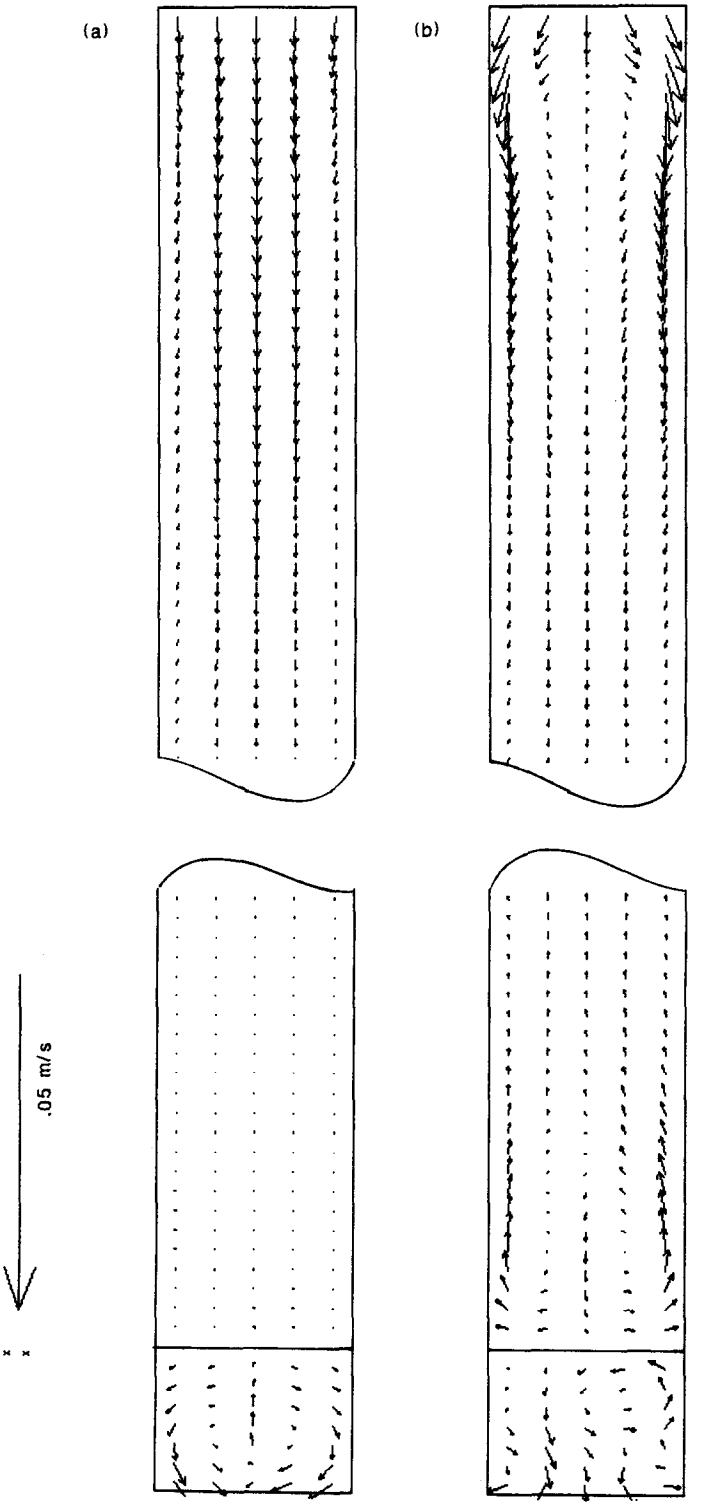

FIG. 10. Velocity vector plot across depth of three-dimensional numerical formulation at lateral distance of $0.25L$ as viewed from the origin: (a) case 5; (b) case 6.

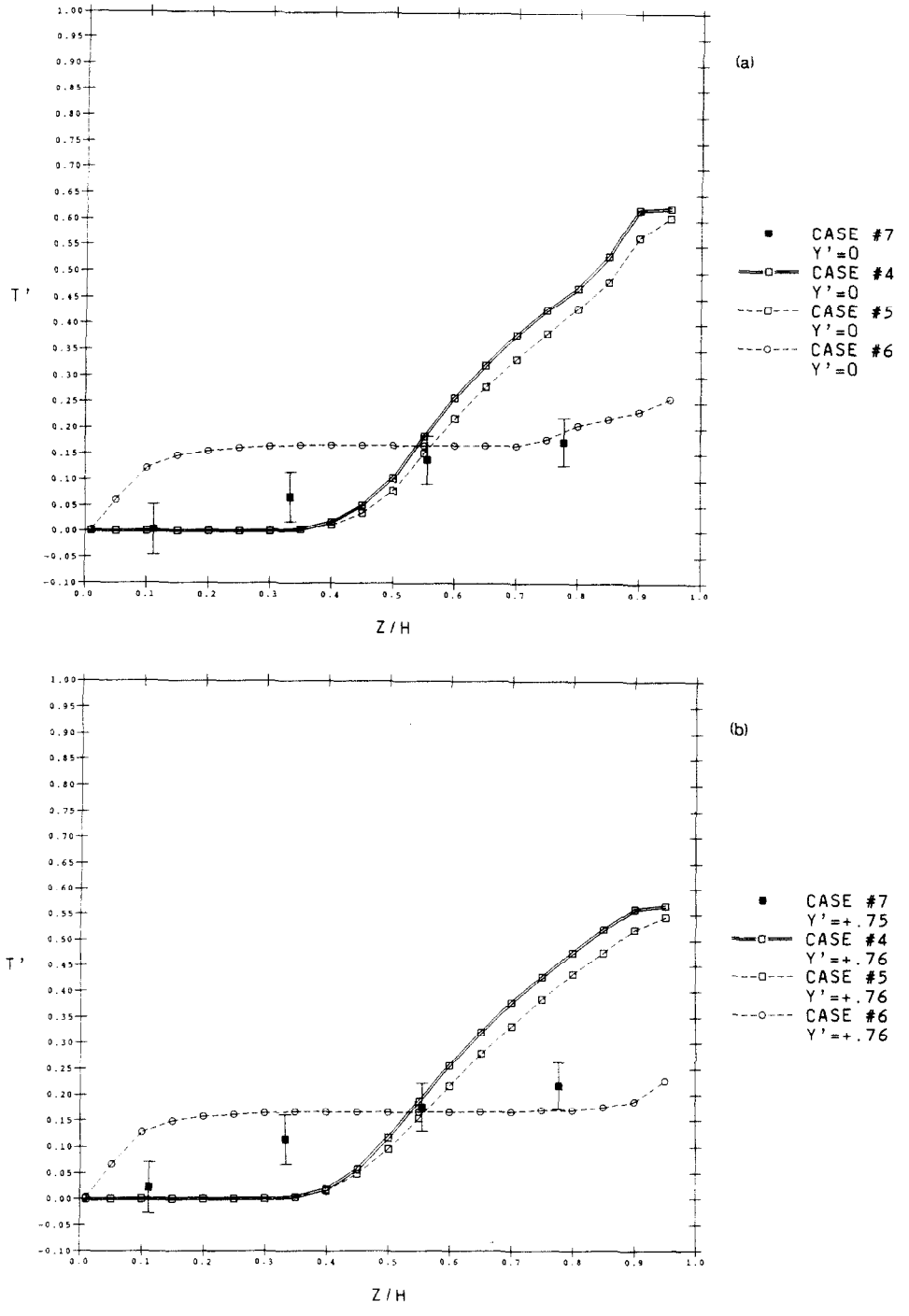

FIG. 11. Non-dimensional temperature vs vertical height for two and three dimensions and experimental data along the Y'-axis at the central plane.

bordered by the two solutions. For constant temperature side walls, the temperature was maintained less than the inlet temperature and greater than the vertical end wall temperature. Average experimental wall temperatures were used as the boundary condition for the side wall temperature in the 3-D numerical formulation of case 6. For this case, the side wall temperature was maintained such that the following relation for comparison to the non-dimensional temperature, T', was satisfied:

$$(T_{IN} - T_{sw}) = T'(T_{IN} - T_w)$$

where $T' = 1/6$.

Comparison of the 2-D case 4 and the 3-D adiabatic

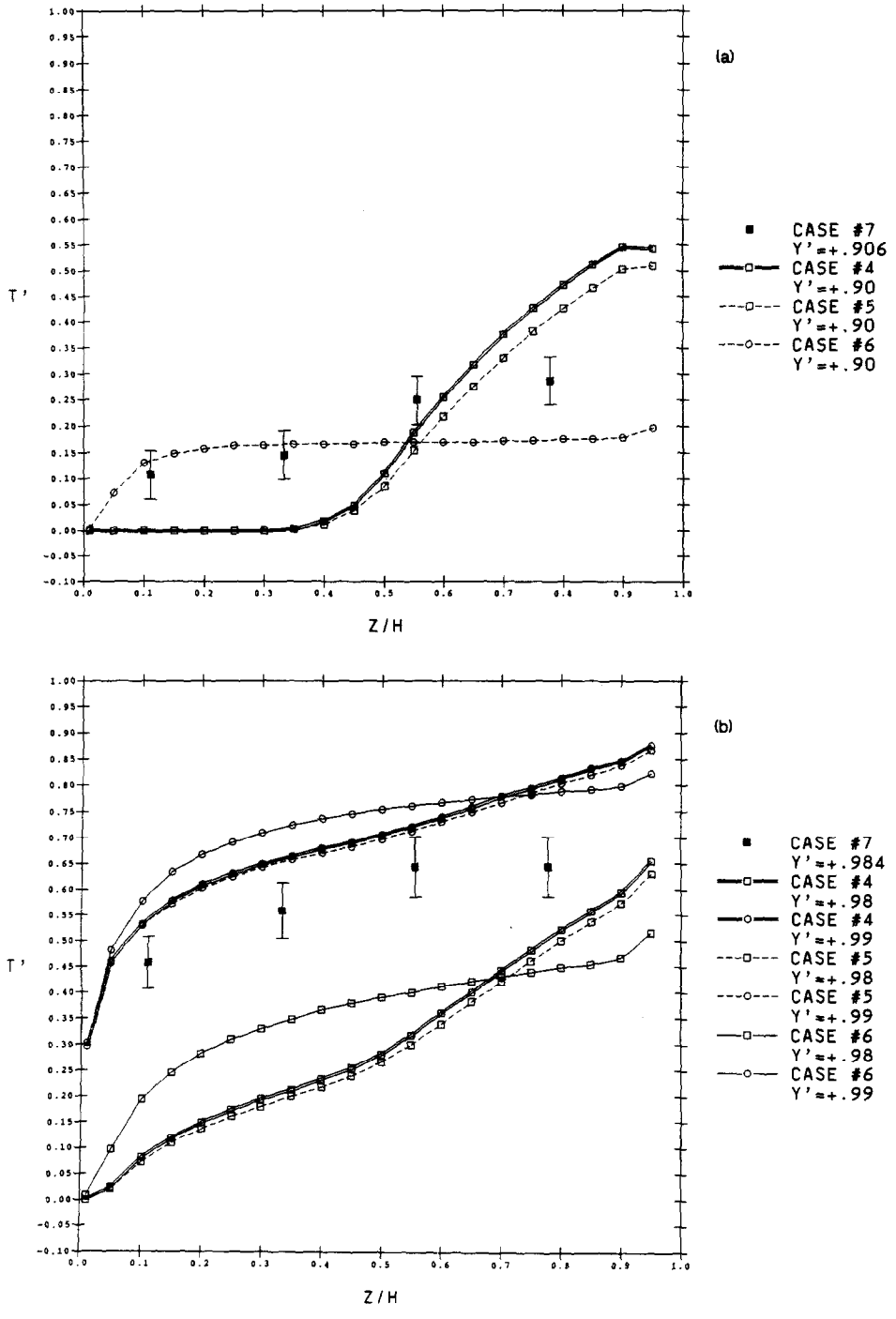

FIG. 12. Non-dimensional temperature vs vertical height for two and three dimensions and experimental data along the Y'-axis at the central plane.

side wall case 5 shows a slight variation in the temperature contour plots (Figs. 6(b) and 7(b)), which was attributed to the increased aspect ratio, A_2, and the additional no-slip boundary condition at the side wall. Comparison of the solution of the 3-D constant side wall temperature case 6 to the 3-D adiabatic side wall case 5 and the 2-D case 4 showed a significant deviation in both the flow structure and temperature profile as shown in Figs. 6–8. This variation between the two 3-D solutions was attributed to differences in the side wall boundary conditions.

Additional effects of the third dimension can be further demonstrated from Figs. 9 and 10. The 3-D adiabatic case 5 differs from the 2-D formulation, case

4, in that the no-slip boundary condition is included along the side walls. The constant temperature side wall case 6 resulted in an increased boundary layer flow that is characteristic of the 'aided' mixed convection flow in a pipe or channel. Case 6 also exhibited flow reversal in areas above the lower baffles and at the inlet. Both cases 5 and 6 showed rotational circulation below the lower baffles.

Non-dimensional temperature profiles for 2-D case 4 and 3-D cases 5 and 6 were compared with the experimental results (case 7) and are shown in Figs. 11 and 12. In these figures, non-dimensional center plane temperatures along the chamber vertical axis are compared at lateral locations along the Y'-axis, where $Y' = 0$ is the centerline of the chamber and $Y' = 1$ is the vertical end wall. The 2-D case 4 consistently overestimated the non-dimensional temperature when compared to the 3-D adiabatic case 5. These differences in non-dimensional temperature were most evident for $Z/H > 0.4$ and were also attributed to the increased aspect ratio, A_2, and the additional no-slip side wall boundary condition. There were significant differences between cases 4 and 5, case 6 and the experimental results (case 7). The experimental results, as expected, agree more with a conduction side wall boundary condition as opposed to the chosen adiabatic or constant temperature boundary conditions. A conjugate numerical formulation to account for the side wall boundary condition for comparison to the experimental results would be more appropriate, but would require a significant increase in computational time.

Verification of the vertical end wall boundary layer thickness was performed using hot wire anemometry measurements. The numerical error in boundary layer thickness was taken to be half of the grid size, ± 0.41 cm, and the experimental error ± 0.32 cm. Anemometer measurements were made by noting a change in the response from the zero baseline and the corresponding location from the vertical end wall was determined to be the boundary layer thickness. This boundary layer thickness as defined was also determined from the numerical solutions of cases 3–6 and the results compared in Table 2 for the vertical non-dimensional locations at $Z/H = 0.44$ and 0.67. The agreement between the experiment and the numerical solution was satisfactory.

The 2-D numerical results of cases 1, 3, and 4 were further analyzed by subdividing the flow structure into three flow types and then determining the volume or area fraction of each flow type within the chamber. The three flow types consisted of short-circuit flow, dead space or diffusion flow, and mixed flow. Table 3 compares these data obtained from the 2-D numerical results to that obtained by Kimmel *et al.* [20] in a similar full-size chamber.

Kimmel *et al.* [20], using techniques developed by Cholette and Cloutier [19], also defined the fraction of the three flow types, but did not consider the temperature variation within the chamber as being a factor in fractionation. To compare the numerical results and the data obtained by Kimmel *et al.* [20], it must also be assumed that the fractionation and development of the three flow types in the inlet and outlet cones are similar to that of the cuboid portion of the chamber. In addition, the numerical results do not address the possibility of an increased fraction of short-circuit flow, and a decrease in dead space and mixed flow fractions due to the two additional walls in the third dimension.

Although the detailed flow structure within the chamber flow cannot be determined by the method of ref. [19] as used by Kimmel *et al.* [20], there is good agreement within the limitations as discussed above for cases 1 and 3 of this study and Kimmel *et al.* [20].

CONCLUSIONS

Development of the chamber flow structure was found to be sensitive to small variations in the temperature difference between the inlet and wall. For positive temperature differences greater than 1°C, the entry above the upper baffles was sufficient such as to provide enough length for the flow to develop and combine in the boundary layer flow. Upper baffle placement in this instance appeared to have a minimal effect upon the development of the resulting flow structure. However, with gradually decreasing temperature differences, the baffle placement had significant impact upon the flow structure, eventually resulting in an asymmetric steady periodic behavior. There were also distinct regions of fluid and energy transport due to either diffusion or convection depending upon the location. With increasing or

Table 3. Percent chamber fraction of defined flow types

Case	Short circuit (convection)	Mixed (mixed convection)	Dead space (diffusion)
1 ($\delta T = 0$°C)	26.0 ± 0.1	65.0 ± 0.2	8.9 ± 0.2
3 ($\delta T = 1$°C)	13.5 ± 0.5	64.4 ± 3.3	25.1 ± 0.7
4 ($\delta T = 3.3$°C)	11.7 ± 0.4	49.2 ± 0.1	39.4 ± 0.1
1 (Kimmel *et al.* [20])†	11.7	64.7	23.6
2 (Kimmel *et al.* [20])‡	27.2	51.3	21.5

† Empty chamber.
‡ Chamber with cages and baffles.

decreasing temperature differentials, these areas were either enlarged or diminished as the flow structure developed, with temperature being the driving parameter.

Use of the laboratory experimental model in the evaluation of the flow structure in the larger, full-size chamber appeared to be limited due to the significant effects of the 3-D geometry. Effects of the additional side wall boundary condition in the 3-D formulation appeared to have a significant effect upon the development of the flow as compared to the 2-D model.

In general, the observed variations in the development of the flow from steady state to oscillatory behavior are consistent with laminar buoyant flow bifurcations for which Prandtl number, geometry, and Rayleigh number are the parameters influencing the flow structure at a specific bifurcation [25]. Variations in the Rayleigh number due to the difference between the inlet and wall temperature in conjunction with either the baffle placement or chamber aspect ratios provided the means for these flow structure transitions to occur. This resulted in the observed differences between the 2-D formulation simulating the full-size chamber, the 3-D formulations and laboratory experimental model.

Acknowledgement—This research was conducted at Wright State University, Dayton, Ohio. Partial support was provided by the Wright Research and Development Center located at Wright–Patterson AFB, Ohio.

REFERENCES

1. S. Ostrach and W. J. Austin, Natural convection in enclosures, *J. Heat Transfer* **110,** 1175–1190 (1988).
2. S. M. Bajorek and J. R. Lloyd, Experimental investigation of natural convection in partitioned enclosures, *J. Heat Transfer* **104,** 527–532 (1982).
3. M. W. Nansteel and R. Greif, Natural convection in undivided and partially divided rectangular enclosures, *J. Heat Transfer* **103,** 623–629 (1981).
4. N. C. Markatos and M. R. Malin, Mathematical modelling of buoyancy-induced smoke flow in enclosures, *Int. J. Heat Mass Transfer* **25**(1), 63–75 (1982).
5. H. Tanaka, S. Maruyama and S. Hatano, Combined forced and natural convection heat transfer for upward flow in a uniformly heated, vertical pipe, *Int. J. Heat Mass Transfer* **30**(1), 165 174 (1987).
6. D. Choudhury and S. V. Patankar, Combined forced and free laminar convection in the entrance region of an inclined isothermal tube, *J. Heat Transfer* **110,** 901–909 (1988).
7. L. S. Yao, Free and forced convection in the entry region of a heated vertical channel, *Int. J. Heat Mass Transfer* **26**(1), 65–72 (1983).
8. S. Ramadhyani, M. Zenouzi and K. N. Astill, Combined natural and forced convective heat transfer in spherical annuli, *J. Heat Transfer* **106,** 811–816 (1984).
9. N. Ramachandran, T. S. Chen and B. F. Armaly, Mixed convection in stagnation flows adjacent to vertical surfaces, *J. Heat Transfer* **110,** 373–377 (1988).
10. D. G. Osborne and F. P. Incropera, Experimental study of mixed convection heat transfer for transitional and turbulent flow between horizontal, parallel plates, *Int. J. Heat Mass Transfer* **28,** 1337–1344 (1985).
11. K. Chiu and F. Rosenberger, Mixed convection between horizontal plates—I. Entrance effects, *Int. J. Heat Mass Transfer* **30,** 1645–1654 (1987).
12. K. Chiu, J. Ouazzani and F. Rosenberger, Mixed convection between horizontal plates—II. Fully developed flow, *Int. J. Heat Mass Transfer* **30,** 1655–1662 (1987).
13. R. L. Carpenter and R. L. Beethe, Cones, cone angles, plenums, and manifolds, *Proc. Workshop on Inhalation Chamber Tech.* (Edited by R. T. Drew), Brookhaven National Laboratory Report BNL 51318 UC-48 (1981).
14. R. O. Moss, A chamber producing uniform concentrations of particulates for exposure of animals on tiers separated by catch pans, *Proc. Workshop on Inhalation Chamber Tech.* (Edited by R. T. Drew), Brookhaven National Laboratory Report BNL 51318 UC-48 (1981).
15. D. R. Hemenway, R. L. Carpenter and O. R. Moss, Inhalation toxicology chamber performance: a quantitative model, *Am. Ind. Hyg. Assoc. J.* **43,** 120–127 (1982).
16. R. L. Beethe, R. K. Wolff, L. C. Griffis, C. H. Hobbs and R. O. McClellan, Evaluation of a recently designed multi-tiered exposure chamber, Department of Energy Contract No. EY-76-C-04-11013 (1979).
17. O. R. Moss, J. R. Decker and W. C. Cannon, Aerosol mixing in an animal exposure chamber having three levels of caging with excreta pans, *Am. Ind. Hyg. Assoc. J.* **43,** 244–249 (1982).
18. H. C. Yeh, G. J. Newton, E. B. Barr, R. L. Carpenter and C. H. Hobbs, Studies of the temporal and spatial distribution of aerosols in multi-tiered inhalation exposure chambers, *Am. Ind. Hyg. Assoc. J.* **47,** 540–545 (1986).
19. A. Cholette and L. Cloutier, Mixing efficiency determinations for continuous flow systems, *Can. J. Chem. Engng* **32,** 105–112 (1959).
20. E. C. Kimmel, K. L. Yerkes and R. L. Carpenter, Design, performance and fluid mechanics of a small animal, whole body inhalation exposure chamber, presented before the 29th Annual Meeting of the Society of Toxicology, 12–16 February, Miami, Florida (1990).
21. S. V. Patankar, *Numerical Heat Transfer and Fluid Flow*, pp. 102–104. Hemisphere, New York (1980).
22. D. B. Spalding, Mathematical modeling of fluid-mechanics, heat transfer and chemical reaction processes, a lecture course, CFDU Report, HTS/80/1, Imperial College, London (1980).
23. Z. Y. Zhong, K. T. Yang and J. R. Lloyd, Variable property effects in laminar natural convection in a square enclosure, *J. Heat Transfer* **107,** 133–138 (1985).
24. TSI Technical Bulletin, Measurements in low velocity gases, TB 14.
25. K. T. Yang, Transitions and bifurcations in laminar buoyant flows in confined enclosures, *J. Heat Transfer* **110,** 1191–1204 (1988).

SIMULATION EXPERIMENTALE ET NUMERIQUE DE CONVECTION MIXTE DANS DE GRANDES CHAMBRES RECTANGULAIRES AVEC BAFFLES

Résumé—On étudie les effets de la convection mixte dans des grandes chambres avec baffles pour des forces de flottement aidées ou opposées. Les résultats expérimentaux et numériques sont comparés pour l'épaisseur de couche limite de quantité de mouvement et pour la distribution de température dans la chambre. Des modèles numériques à deux et trois dimensions sont formulés par un schéma implicite aux différences finies. Les températures d'entrée et de paroi sont maintenues constantes tandis que la vitesse d'entrée est uniforme. Deux tiers des quatre (deux par tiers) baffles horizontaux sont logés de façon axisymétrique autour de l'axe vertical avec l'entrée au sommet et la sortie à la base de la chambre. La différence entre les températures d'entrée et de paroi varie entre $-1{,}0$ et $3{,}3$ C avec un nombre de Prandtl $Pr = 0{,}7$, un nombre de Reynolds d'entrée $Re = 32$ et 235, un nombre de Rayleigh d'entrée $Ra = 0$–$6{,}8 \times 10^7$. On conclut que l'écoulement est principalement flottant et par nature asymétrique. Le développement de l'écoulement est sensible aux petites variations de différence de température entre l'entrée et la paroi.

EINE EXPERIMENTELLE UND NUMERISCHE SIMULATION DER MISCHKONVEKTION IN EINER GROSSEN RECHTECKIGEN KAMMER MIT UMLENKBLECHEN

Zusammenfassung—Der Einfluß der Mischkonvektion in einer großen Kammer mit Umlenkblechen wird für die Fälle gleichgerichteter und gegengerichteter Auftriebskräfte untersucht. Die experimentellen und die numerischen Ergebnisse werden im Hinblick auf die Dicke der Strömungsgrenzschicht und die Temperaturverteilung in der Kammer verglichen. Mit Hilfe eines vollständig impliziten Finite-Differenzen-Verfahrens wird ein zwei- und ein dreidimensionales transientes Modell für laminare Strömung formuliert. Die Eintritts- und die Wandtemperaturen werden konstant gehalten, die Eintrittsgeschwindigkeit ist gleichförmig. Zwei Reihen mit jeweils zwei waagerechten Umlenkblechen sind achsensymmetrisch um die senkrechte Achse angeordnet, wobei sich der Eintritt an der Oberseite und der Austritt an der Unterseite der Kammer befinden. Die Differenz zwischen Eintritts- und Wandtemperatur liegt zwischen $-1{,}0$ und $3{,}3$ C, die Prandtl-Zahl beträgt $Pr = 0{,}7$ die Reynolds-Zahl am Eintritt $Re = 32$ und 235, die Rayleigh-Zahl am Eintritt liegt zwischen $Ra = 0$ und $6{,}8 \times 10^7$. Als Schlußfolgerung ergibt sich, daß die Strömung hauptsächlich auftriebsbestimmt und asymmetrisch ist. Die Entwicklung der Strömung hängt stark von kleinen Schwankungen der Temperaturdifferenz zwischen Eintritt und Wand ab.

ЭКСПЕРИМЕНТАЛЬНОЕ И ЧИСЛЕННОЕ МОДЕЛИРОВАНИЕ СМЕШАННОЙ КОНВЕКЦИИ В БОЛЬШИХ ПРЯМОУГОЛЬНЫХ КАМЕРАХ С ПЕРЕГОРОДКАМИ

Аннотация—Исследуются эффекты смешанной конвекции в больших камерах с перегородками при действии подъемных сил как в одинаковом, так и в противоположных направлениях. Сравниваются экспериментальные и численные результаты для течения в пограничном слое и распределения температур в камере. С использованием полностью неявной конечно-разностной схемы построены двух- или трехмерные нестационарные ламинарные численные модели. Температура на входе и температура стенки поддерживались постоянными при сохранении равномерной скорости на входе. Два ряда из четырех (двух в каждом ярусе) перегородок располагались асимметрично относительно вертикальной оси, причем вход размещался у верхней поверхности камеры, а выход—у ее основания. Разность температур между входом и стенкой колебалась в пределах $-1{,}0$–$3{,}3$°C при числе Прандтля $Pr = 0{,}7$, числе Рейнольдса на входе $Re = 32$ и 235 и числе Рэлея на входе $Ra = 0$–$6{,}8 \times 10^7$. Сделан вывод о том, что течение является преимущественно свободноконвективным и асимметричным. Развитие течения весьма чувствительно к небольшим изменениям разности температур между входом и стенкой.